

1 Characterisation of nano-scale precipitates in BOR60 irradiated T91 steel using atom probe
2 tomography

3 Guma Yeli^{1,2*}, Victoria C.I. Strutt¹, Maria. A. Auger^{1,3}, Paul A.J. Bagot¹, Michael P.
4 Moody^{1*}

5 ¹Department of Materials, University of Oxford, Parks Road, Oxford, OX1 3PH

6 ²Centre for Advanced Nuclear Safety and Sustainable Development, City University of
7 Hong Kong, Hong Kong, China

8 ³ Department of Physics, Universidad Carlos III de Madrid, Leganés, Madrid, Spain

9

10 *Corresponding author:

11 Guma Yeli, gumayeli@cityu.edu.hk, Centre for Advanced Nuclear Safety and
12 Sustainable Development, City University of Hong Kong, Hong Kong SAR

13 Michael P. Moody, michael.moody@materials.ox.ac.uk, Department of Materials,
14 University of Oxford, Parks Road, Oxford. OX1 3PH

15

16 Highlights

- 17 • T91 steel was irradiated in BOR60 reactor at five different temperature/dose
18 conditions.

- The number density, volume fraction, size and composition of the early stage Mn, Ni, Si -rich clusters have been characterised by atom probe tomography.
- After irradiation, Ni, Mn, Si and P segregation to carbide/matrix interface has been observed.
- Fe clustering inside a carbide was observed after irradiation at 524 °C:15.4dpa, which has not been reported before.

Abstract

Atom probe tomography has characterised the microstructural changes in T91 steel after BOR60 reactor irradiation at five temperatures between 376 °C and 524 °C to doses between 14.6 dpa and 35.1 dpa. Irradiation-induced precipitation and segregation to carbide/matrix interface induced by neutron irradiation has been characterised. Atom probe tomography characterisation shows that Mn, Ni, Si -rich (MNS-rich) clusters form in T91 steel irradiated in BOR60 reactor at temperatures between 376 °C and 415 °C, which is not observed at higher temperatures 460 °C and 524 °C. The number density, volume fraction and composition of MNS-rich clusters have been characterised. Ni, Mn, Si and P is found to segregate at carbide matrix interface after irradiation at lower temperature and only P segregation is observed at 524 °C.

Keywords: T91 steel, BOR60 reactor, MNS-rich clusters, atom probe tomography

38 1 Introduction

39 One of the key factors for safe operation of current reactors and implementation of
40 advanced nuclear energy systems is the long term stability of structural components
41 exposed to a combination of both high temperature and high neutron flux [1]. To this
42 end, ferritic/martensitic (F/M) steels are appealing structural materials for high dose
43 structural components because of their outstanding resistance to radiation-induced
44 swelling, high thermal conductivities and low thermal expansion coefficients [2–4].

45

46 Among various commercial F/M steels, T91, a modified 9Cr-1Mo steel has found a
47 rising number of applications as a structural material for fission reactors in recent years.
48 However, prolonged exposure to neutron irradiation drives microstructural evolution in
49 T91 steel, which has detrimental effects on the mechanical properties. For example,
50 irradiation can alter the distribution and composition of the pre-existing carbide/nitrides.
51 In their tempered state, the main precipitates in F/M steels are carbides and/or nitrides
52 [5–7]. The pre-existing carbides and nitrides contribute to strengthen the material and
53 are expected to be stable under service conditions. However, research has shown that
54 modification of structure, density, size and composition of pre-existing precipitates can
55 occur when exposed to irradiation [8–10]. $M_{23}C_6$ was previously shown to increase in
56 size and grain boundary coverage in an 11Cr F/M steel after neutron irradiation at
57 temperatures between 500 °C - 650 °C [10]. Amorphization of $M_{23}C_6$ carbides has been

observed in various F/M steels exposed to neutron irradiation [5,11]. The composition of the carbides can also be altered by irradiation [12]. In T91 steel, when the ion irradiation dose increased from 1 dpa to 10 dpa, the carbide size first slightly increased and then decreased [13]. Radiation induced segregation (RIS) of solutes to grain boundaries has been observed in F/M steels. Jiao et al. [14] using scanning transmission electron microscopy (STEM) studied RIS in a set of T91 steel samples subject to a range of irradiation conditions in the BOR60 fast research reactor. Their analyses showed a temperature dependence of RIS magnitude.

In addition to the modification of pre-existing carbide/nitride precipitates and RIS, the local solute concentration in the vicinity of a defect sink can reach the solubility limit, leading to radiation-induced precipitation. In T91, Mn, Ni, Si -rich (MNS-rich) clusters are known to form under irradiation, leading to embrittlement [9,14–24]. Various studies on MNS-rich clustering specific to T91 have been carried out using a variety of characterisation techniques to investigate a range of irradiation conditions. Table 1 summarises results in the literature from previous studies measuring number density, volume fraction and averaged diameter of MNS-rich precipitates resulting from different irradiation experiments. In addition to investigating RIS, in the same BOR 60 irradiated T91 samples Jiao et al. [14] used TEM to measure the number density of MNS-rich precipitates to be in the order of 10^{21} m^{-3} . T91 samples proton irradiated to

7 dpa at 400 - 500 °C ([25]) have also been shown to produce MNS-rich precipitates and copper-rich precipitates (CRPs). The absence of MNS-rich precipitates under a lower proton irradiation dose in the same study suggests that the cluster formation is enhanced by irradiation. Analysis of neutron irradiated T91 by several methods suggests an increase in diameter as temperature and dose are increased.

Table 1 Summary of MNS-rich precipitates analysis in T91 from literature. d = averaged diameter, f = volume fraction and N = number density.

Study:	Technique	Irradiation	Conditions	d (nm)	f (%)	N (m ⁻³)
Jiao [14]	TEM	BOR60-neutron	17.1dpa,376°C	5.8	0.037	3.6×10^{21}
			35.1dpa,378°C	7.0	0.043	2.4×10^{21}
			18.6dpa,415°C	6.7	0.047	3.0×10^{21}
Jiao [12]	TEM	Proton-2MeV	7dpa, 400°C	4.4	/	1.27×10^{23}
			7dpa,500°C	8.0	/	0.14×10^{23}
Pareige [26]	APT	Self-ion irradiated	0.5dpa, 300°C	3.0	/	2.8×10^{23}
			0.5dpa, 420°C	3.8	/	0.52×10^{23}
Kuksenko [27]	APT	MTR-neutron	0.6dpa, 300°C	3.2	/	2.4×10^{23}
Wharry [25]	APT	Proton-2MeV	7dpa, 400°C	4.1	/	7.4×10^{22}

From the literature, behaviour of MNS-rich precipitates in T91 under both neutron and ion irradiation is inconclusive. In particular, the compositional analysis of MNS - precipitates is lacking. To further understand and determine the suitability of T91 for generation IV reactors, compositional analysis on the nanoscale and a correlative view of how this affects materials properties is required. An integrated research project (IRP)

has been initiated between different universities and research institutes in US and UK. A fuller description of this project can be found in [28]. One of the main goals of the program was to understand the microstructural evolution of T91 steel under reactor irradiation. The main aim of the present study is to better understand the nano-scale MNS-rich cluster formation at different temperatures and doses and provide compositional data of the irradiated microstructure. As such, [atom probe tomography \(APT\)](#) analyses were carried out to study the microstructure of T91 steel subjected to BOR60 reactor irradiation. The MNS-rich cluster formation, carbide/nitride compositions and solute segregation on the carbide/matrix interface have been examined. The temperature dependence of cluster formation and solute segregation have been characterised and the results are compared with the STEM results from Jiao et al. [14] and previous data from the literature.

2 Materials and Experimental Methods

All APT analyses were carried out on a Cameca LEAP 5000 XR instrument. Voltage pulsing mode with a 20 % pulse fraction was utilised for the atom probe experiments. The specimen temperature and pulse repetition rate were set to 50 - 55 K and 200 kHz, respectively. CAMECA IVAS software was used to reconstruct the detected information into 3D positions and chemical identity of each ion.

T91 steel used in this study was received from Pacific Northwest National Laboratory (PNNL). As-received T91 steel sample for APT analyses were prepared from 3 mm TEM disks after diamond lapping to 0.25 μm at the University of Michigan. The composition of as-received T91 measured by APT and chemical composition provided by PNNL are both listed in Table 2. Compared to the bulk chemistry, the Cr and V contents are lower in APT measurements. The loss of Cr and V is about 1.25 at. % and 0.09 at. % respectively. Also, the majority of the expected Nb, C and N atoms were not detected in the APT analysed regions. The loss of these elements in the composition measurement is most likely due to the formation of nitrides and carbides outside the analysed region. From previous studies, Cr-rich carbide (~ 100 nm) were present along prior austenite grain boundaries (PAGBs) and lath boundaries. The finer V, Cr- rich nitrides (~ 40 nm) were both in the matrix and adjacent to the carbides [12]. Due to the small analysed volumes by APT, such large carbides/nitride were not captured in any of the as-received T91 data. Hence, it is not surprising that contents of carbide/nitride formers obtained via APT are lower.

Table 2 Composition of T91 from APT and bulk composition provided by PNNL. The error in APT composition is obtained by averaging data from three different analysed specimens.

	Alloy Chemistry (at. %)									
	Cr	Ni	C	N	Mn	Mo	Nb	Si	V	Fe
Bulk composition provided by PNNL	9.16	0.08	0.37	0.21	0.37	0.51	0.04	0.22	0.23	Bal.
Composition measured via APT	7.91	0.10	0.04	0.05	0.40	0.40	-	0.27	0.14	Bal.
Error (±)	0.05	0.02	0.01	0.05	0.04	0.04	-	0.05	0.06	-

The neutron irradiations were conducted in the BOR60 test reactor in Russia. Due to the radioactive nature of the resulting samples, lamellas were made using a lift-out process [29] for BOR60 irradiated T91 at the Low Activation Materials Development and Analysis (LAMDA) laboratory at Oak Ridge National Laboratory (ORNL). A dual beam microscope FEI Helios NanoLab 600i at Culham Centre for Fusion Energy (CCFE) was used to prepare BOR60 irradiated T91 for APT analysis. The unirradiated T91 specimen were also prepared using the FEI Helios Nano Lab 600i at CCFE. A detailed description of BOR60 irradiation conditions and methods for dose and temperature calculation can be found in Ref. [14]. The average irradiation temperatures and the accumulated irradiation doses at retrieval were calculated as 376 °C:17.1dpa (irradiation temperature: final irradiation dose), 378 °C:35.1dpa, 415 °C:18.6dpa, 460 °C:14.6dpa and 524 °C:15.4dpa. The dose rate was $6 - 9 \times 10^{-7}$ dpa/s. The neutron damage profile is relatively flat. All the BOR60 irradiated samples were taken from a depth between 200 - 600 nm from the surface.

141

142 In the reconstructed APT data, the identification and characterisation of Mn, Ni, Si -
143 rich clusters was undertaken [based on the maximum separation method](#) [30,31]. In
144 simple terms, the distance separating a solute atom (defined as Ni, Si and Mn in this
145 case) from its K^{th} (10^{th} in this study) nearest solute neighbour is measured within the
146 data. If this distance is less than a defined value, d_{max} , the two solute atoms are
147 determined to be “core” of the same cluster. Any cluster containing less than a defined
148 number of atoms, N_{min} , is removed from the analysis to remove contributions from very
149 small clusters statistically likely to form from random fluctuations in the matrix. After
150 solute clusters are defined, matrix atoms within a distance L , of the clustered solute
151 atoms, are included in the cluster. This selection of atoms is then eroded back a distance
152 of E (erosion parameter). The parameters chosen to define the maximum separation
153 were $d_{max} = 0.7$ nm, $N_{min} = 20$ atoms, $L = e = 0.5$ nm. The number density, N , of clusters
154 identified within the reconstruction was calculated using the following formula:

$$N = \frac{n\eta}{N_{tot}\Omega} \quad (1)$$

155 where n is the total number of clusters and N_{tot} is total number of atoms in the analysed
156 volume, Ω is the volume of one solute atom, taken as 1.094×10^{-2} nm³, assuming the
157 solutes have a similar atomic volume as Ni. η is the ion detection efficiency of the atom
158 probe instrument, which has been estimated to be 0.52 for the LEAP 5000 XR. The

159 volume fraction of clusters is an important factor to estimate their influence on strength
160 and hardness. The volume fraction, f , is estimated by:

$$f = \frac{\sum_{i=1}^n N_{sol}}{N_{tot}} \quad (2)$$

161 where N_{sol} is the total number of solute atoms incorporated within a cluster.

162 The radius, r , of a precipitate was equated to that of the volume equivalent sphere:

$$r = \sqrt[3]{\frac{3N_{sol}\Omega}{4\pi\eta}} \quad (3)$$

163 Excluding the matrix atoms could lead to under-estimation of the size and volume
164 fraction. However, previous studies have provided evidence that the majority of Fe
165 atoms in the clusters, as observed by APT, are due to trajectory aberrations [32]. Hence,
166 the systematic method described above was used to estimate the volume fraction f and
167 radius r .

168 3 Results

169 3.1 As-received T91

170 Three tip-shaped specimens of as-received T91 steel were analysed. The obtained
171 datasets included 33.0M, 7.2M and 17.1M ions, respectively. Atom maps of individual
172 elements from Tip 1 are shown in Figure 1. Atom maps from Tip 2 and Tip 3 are
173 included in the supplementary materials. Precipitates enriched with V, Cr and VN ions
174 are observed in the as-received T91 samples. From compositional analysis (included in

the supplementary materials), the precipitates contain approximately 40 at. % V, 20 at. % Cr and 30 at. % N. Other elements are homogenously distributed in the matrix. CrC ions are also found at the bottom edge of the tip.

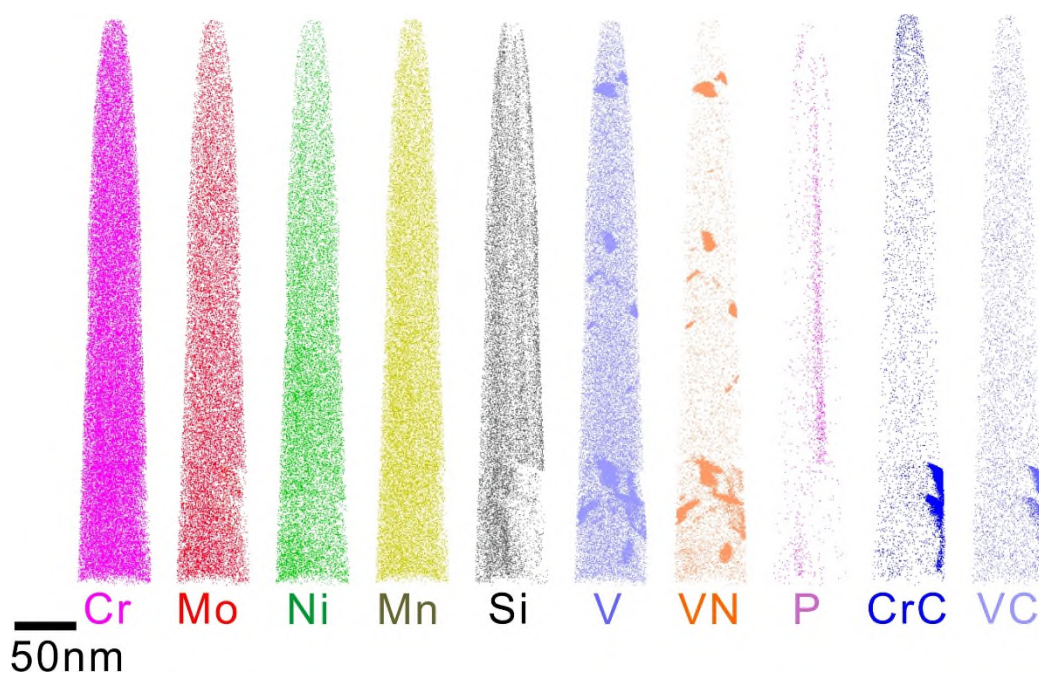


Figure 1 Atom maps of individual elements, nitride and carbide ions in as-received T91

3.2 Elemental distributions of T91 steel irradiated in BOR60

From each irradiation condition, 2 - 4 needles were analysed using APT. Datasets including between 2.2M - 12.4M ions were analysed. Figure 2 (a) - (e) presents the APT atom maps obtained from the analysis of T91 steel irradiated in BOR60 at the different conditions. Compared to the unirradiated T91, the V-rich nitride particles were not observed in any T91 specimen after irradiation. In all the specimen irradiated at temperature ranges between 376 °C and 415 °C, distinct solute clusters containing Ni,

Mn, and Si were detected. However, such clusters were not observed when the temperature was raised to 460 °C and 524 °C, respectively. Cu and P was also found to cluster together with some of these MNS-rich clusters. As shown in Figure 1, this clustering was not present in the as-received T91.

Cr-rich carbide particles were also captured in some specimens, i.e. Figure 2 (a), (c) and (e). A range of behaviours were observed with respect to the incorporation of these carbides. Ni, Si, Mn and P was found to segregate to the carbide/matrix interface at 415 °C (Figure 2 (c)), whereas at the higher temperature of 524 °C, only P was found to segregate to the interface (Figure 2 (e)). Mn was found to be enriched inside the carbide at 524 °C. As shown in Figure 2 (e), Fe appeared to deplete at the interface and cluster inside the carbide. Clustering of Fe inside the carbide has not been well-documented. V-rich nitride particles were also observed inside the carbide. Except from the specimen containing carbides (i.e the one in Figure 2 (e)), solute elements were found to be randomly distributed after irradiation at higher temperatures (460 °C and 524 °C).

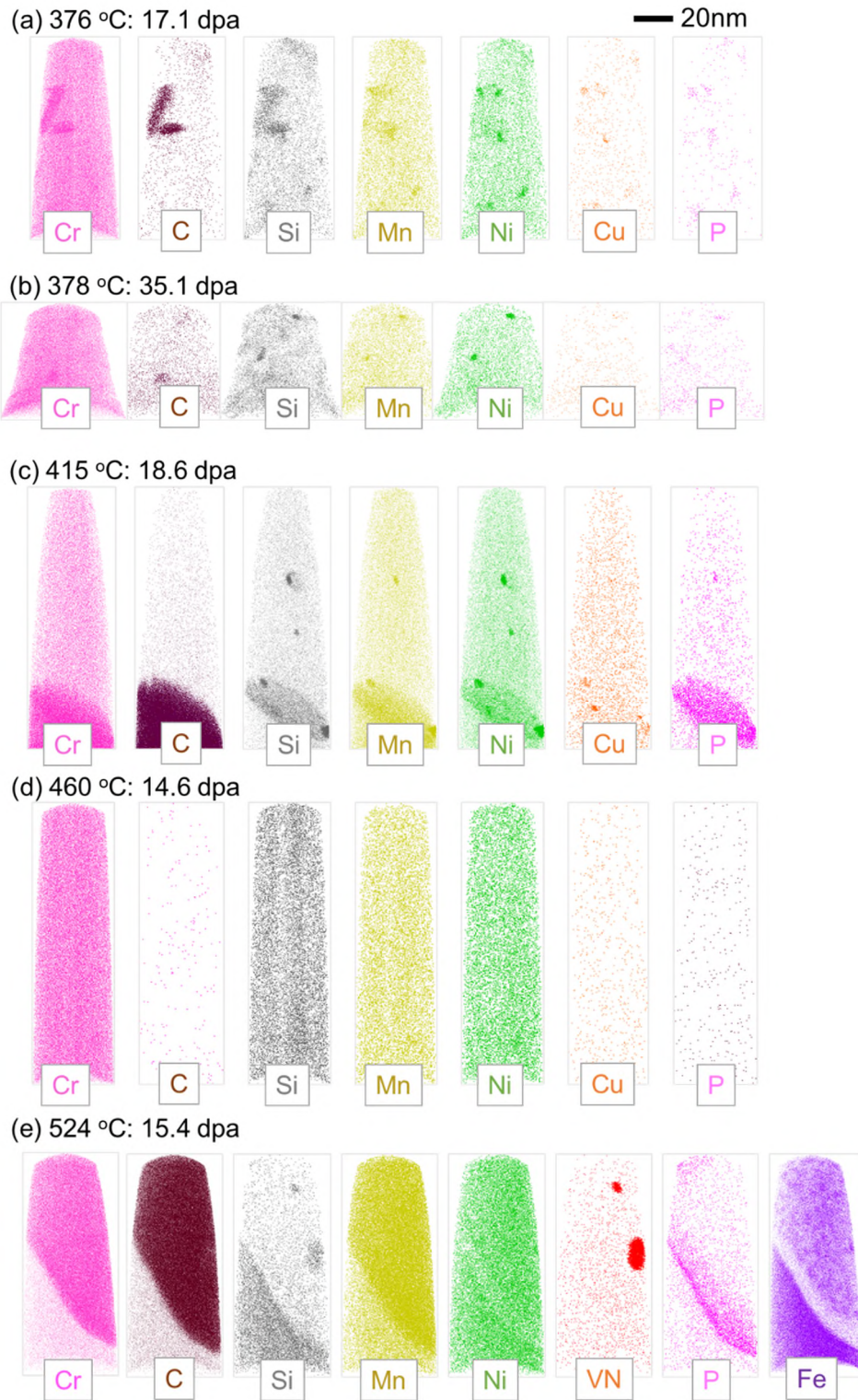


Figure 2 Atom maps of T91 steel irradiated in BOR60 (a) 376 °C:17.1dpa, (b) 378 °C:35.1dpa, (c) 415 °C:18.6dpa, (d) 460 °C:14.6dpa and (e) 524 °C:15.4dpa. Note that due to the mass-to-charge-state ratio overlap at 14 and 15 Da, which for the purposes of this figure have been assigned to be Si, the majority of the Si enrichment associated to the carbide and nitride are in fact misidentified N ions

3.3 Number density, volume fraction and composition of MNS-rich precipitates

The MNS-rich precipitates were analysed using methods described in Section 2. Table 3 presents the measured number density, N , volume fraction, f , and averaged diameter, d , of the clusters at different irradiation conditions. The error is obtained by averaging the results of the analyses across multiple APT reconstructions. It needs to be pointed out that there are still systematical errors caused by the selection of cluster analysis parameter. The same data analysis parameters were used to minimize the effect of cluster selection parameters when comparing between datasets. The measured number densities were all in the order of $10^{23}/\text{m}^3$. It should be noted that, due to the relatively small volumes of microstructure sample in each APT and the limited number of clusters observed that the uncertainty of the number density, volume fraction and diameter might be quite large. This is consistent with the observations from atom maps such that even at the same irradiation condition, the distributions of clusters vary significantly analysis to analysis. Hence, no clear trend with temperature and dose level can be ascertained when considering the relatively large error. When the irradiation temperature was higher than 460 °C, no clusters were identified using the same search algorithm applied to all the APT data.

Table 3 Number density (N), volume fraction (f) and diameter (d) of MNS-rich precipitates. The error is obtained by averaging different specimen at the same irradiation condition.

Alloy	$N (\text{m}^{-3})$	\pm	$f (\%)$	\pm	$d (\text{nm})$	\pm
376 °C:17.1dpa	1.37E+23	4.66E+22	0.12	0.04	2.0	0.5
378 °C:35.1dpa	3.00E+23	4.34E+22	0.09	0.06	1.8	0.4
415 °C:18.6dpa	1.53E+23	6.05E+22	0.09	0.1	1.8	0.5

460 °C:14.6dpa & 524 °C:15.4dpa	-	-	-	-	-	-
--	---	---	---	---	---	---

Table 4 lists the concentration of the main elements in MNS-rich clusters formed after BOR60 irradiation in T91. When the irradiation dose was increased from 376 °C:17.1 dpa to 378 °C:35.1 dpa, the Ni and Mn contents were very similar. However, the Si content in the clusters almost doubled, increasing from 6.9 at. % to 13.3 at. %. It has previously been reported that Si has the highest affinity for vacancies compared to Ni and Mn [33]. At higher doses, the number of defects is higher than that of lower dose level. Thus it is not surprising that the clusters at 378 °C:35.1dpa are more enriched in Si.

Table 4 The averaged concentration of the main elements in NMS-rich clusters. The uncertainty is the standard error of different clusters.

Alloy	Composition (at. %)						
	Ni	Si	Mn	Cu	Fe	Cr	P
376 °C:17.1dpa	11.9±4.5	6.9±4.8	8.0±2.4	0.6±0.4	61.1±9.5	8.0±3.2	0.4±0.4
378 °C:35.1dpa	11.8±5.5	13.3±5.9	8.1±2.8	0.2±0.4	56.6±8.5	8.6±5.1	0.3±0.5
415 °C:18.6dpa	12.4±5.3	11.1±6.3	7.4±2.7	0.2±0.4	59.4±9.2	8.7±3.8	0.3±0.5

3.4 Carbide composition

As shown in Figure 2 (c) and (e), large (several tens of nm) carbide particles were captured in the APT analyses of BOR60 irradiated T91. A close-up of elemental distributions and a 1D concentration profile across the matrix-particle interface in T91 irradiated at 415 °C:18.6dpa is shown in Figure 3. The carbide particle is enriched in Cr, Mo and C. The composition matches $M_{23}C_6$ type carbide. Ni, Si, Mn and P is observed to segregate to the carbide/matrix interface. The peak concentration of Ni, Si and Mn is all around 2.5 at. % at the interface and P content is ~ 1 at. %.

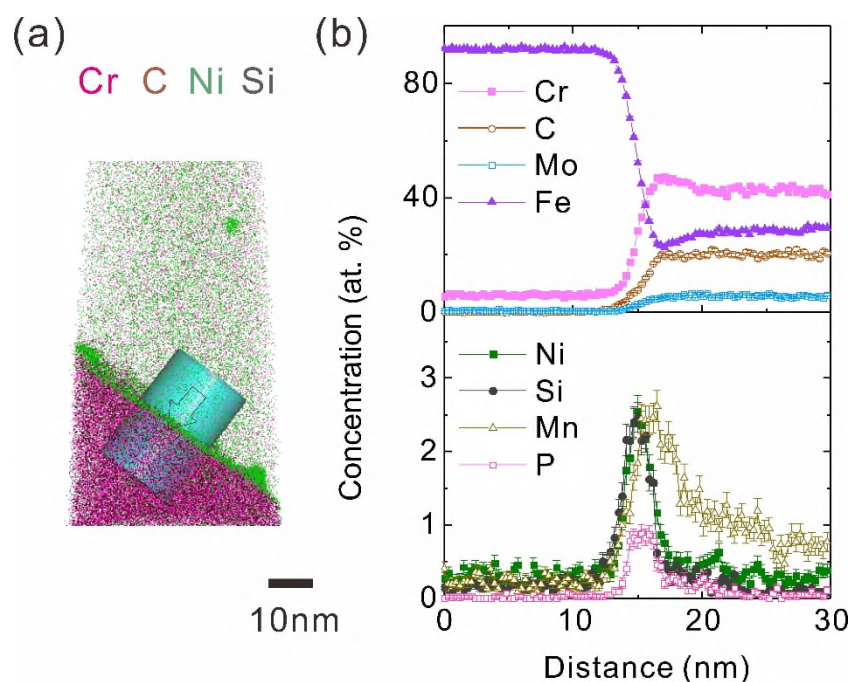


Figure 3 (a) Close-up of atom maps at the carbide/matrix interface in BOR60 irradiated T91 at 415 °C:18.6dpa. The analysed sample is the same as in Figure 2 (c); (b) 1 D concentration profile across the interface

When the irradiation temperature was raised to 524 °C, as shown in Figure 4, only P segregation was observed at the carbide/matrix interface. Instead of segregation at the interface, Mn was enriched by ~ 1 at. % inside the carbide and Si was rejected from it. Also, an Fe depleted zone was observed near the interface. Then Fe content increased again inside the carbide. This is due to the formation of small Fe-rich clusters inside the carbide particle. These Fe-rich clusters are highlighted using 40 at. % Fe isoconcentration surface in Figure 5 (a) and the concentration proxigram is displayed in Figure 5 (b). The clusters are 2 - 3 nm in radius and the Fe content in the core regions exceeds 80 at. %. The formation of Fe-rich clusters inside the carbide particles in this material has not been reported before.

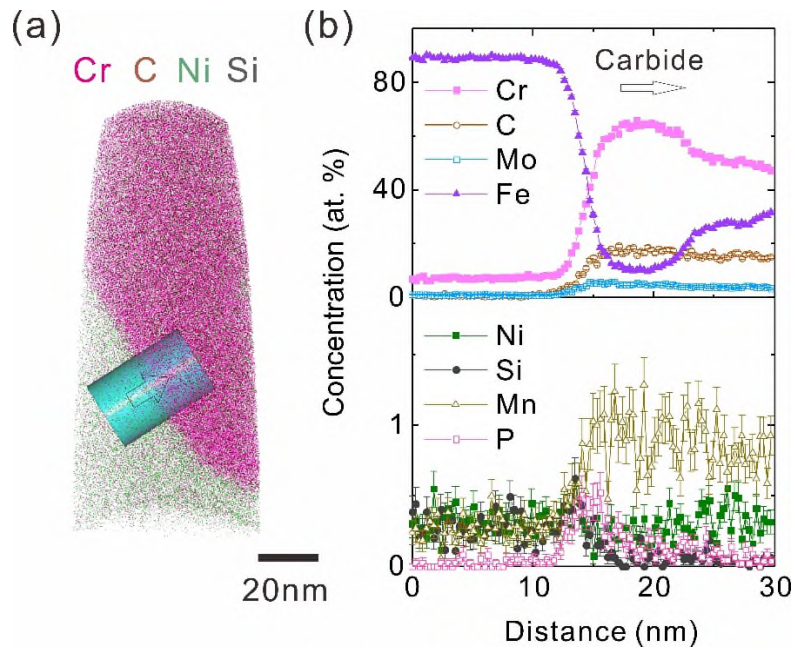


Figure 4 (a) Close-up of atom maps at the carbide/matrix interface in BOR60 irradiated T91 at 524 °C:15.4dpa. The analysed volume is the same as in Figure 2 (e); (b) 1 D concentration profile across the interface

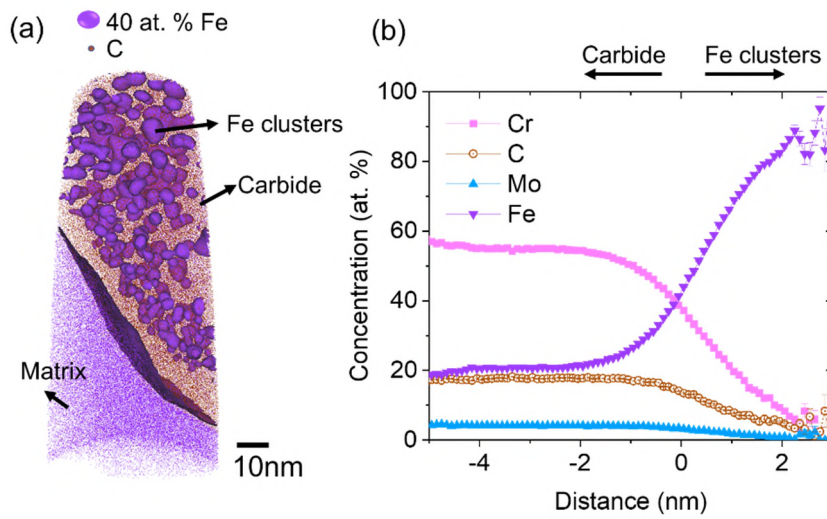


Figure 5 (a) 40 at. % Fe isoconcentration surface in BOR60 irradiated T91 at 524 °C:15.4dpa. The analysed volume is the same as in Figure 2 (e); (b) Averaged concentration proxigram across the 40 at. % Fe isoconcentration surface

4 Discussion

4.1 MNS-rich cluster formation

Distinct MNS-rich clusters were observed in all the samples irradiated below 415 °C. MNS clusters were not observed at 460 °C and 524 °C. The results from APT analysis are consistent with the STEM observation on the same set of materials, even though a clear grain boundary segregation of Ni and Si is observed at 460 °C [14]. From Table 1, the radius of the detected clusters by TEM was 5 - 7 nm, with a number density in the order of 10^{21} m^{-3} . In the present study, the averaged diameter and number density obtained via APT were $\sim 2 \text{ nm}$ and $\sim 10^{23} \text{ m}^{-3}$, respectively. The size measured by APT is much smaller than that of TEM and the number density is much higher. In the present study, matrix atoms were excluded to calculate the cluster size. This is based on the findings of previous studies which lead to the assumption that most matrix atoms incorporated into the detected MNS-rich clusters in this steel arise from trajectory aberration and limitations of the atom probe image reconstruction protocols [32,34]. Another possible reason is the difference in resolution limits of TEM compared to APT. It is highly likely that larger clusters occurring with lower number density measured via TEM are in fact present in the specimen studied here, but were statistically unlikely to be captured in the APT analyses due to its more limited sampling volume. Conversely, the much more abundant very small clusters detected via APT were not seen in TEM. These two techniques can be complementary to better understand irradiation induced

damage in materials and to underpin modelling efforts with microstructural data across a range of scales.

In this study APT analyses have characterised the compositions of MNS-rich clusters in T91. Previously Gupta [35] summarised several stable MNS-rich phases, namely G ($\text{Mn}_6\text{Ni}_{16}\text{Si}_7$), E (MnNiSi), Γ_1 ($\text{Mn}_3\text{Ni}_3\text{Si}_2$), Γ_2 ($\text{Mn}_2\text{Ni}_3\text{Si}_2$), Ω ($\text{Mn}_3\text{Ni}_2\text{Si}$). Among them, G phase and Γ_2 phase have been reported to be thermally stable in various RPV steels [36–39]. Figure 6 summarises the Ni-Mn-Si relative composition of all the detected MNS-rich clusters in T91. The radius of each circle indicates the size of the corresponding cluster. In the present study, since the clusters are still in their early stage of formation, a large scatter is observed in cluster composition at all the irradiation conditions. Compared to the known Mn-Ni-Si phase, the composition of small clusters was closer to Γ_2 phase. However, the larger clusters contain more Ni than the smaller ones and the composition shifted away from Γ_2 . The larger precipitates possessed a Ni-Mn-Si composition closer to G-phase. The Ni-Mn-Si relative composition of the larger clusters were ~ 54 at. % Ni, 30 at. % Si and 16 at. % Mn. The Si content in the large clusters was still slightly higher than that of G phase and Mn content is slightly lower. Thus the clusters are likely precursors of G phase.

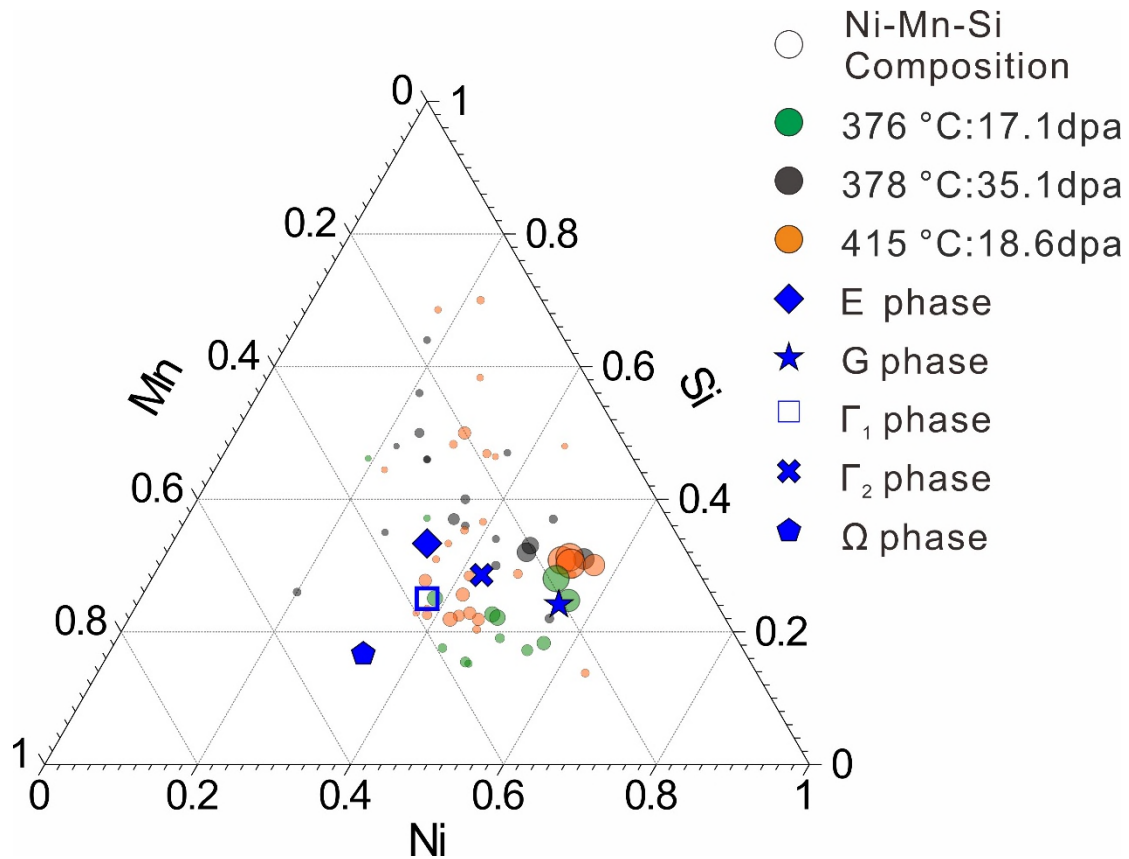


Figure 6 Gibbs triangle plot of APT Mn-Ni-Si compositions observed in BOR60 compared to known MNS phase

4.2 Carbide matrix interface

In Figure 2 (c), a clear Ni, Mn, Si and P segregation to carbide matrix interface is seen in BOR60 irradiated T91 at 415 °C:18.6dpa. At higher temperature 524 °C, only P segregation was observed (Figure 2 (e)). The magnitude of depletion/enrichment are given in Table 5. At 415 °C Ni, Si, Mn and P at the observed grain boundary were enriched by 2.1 at. %, 2.2 at. %, 2.0 at. % and 0.8 at. %, respectively. At higher temperature 524 °C, the segregation of Ni, Si and Mn was not observed and the P segregation was decreased to 0.4 at. %. The grain boundary segregation of Ni and Si

on the same sample has been studied using STEM in Reference [14]. The magnitude of RIS of Ni and Si peaked around 415 °C and decreased at higher temperatures. At 524 °C, no clear segregation of Ni and Si was observed using STEM. Results from the APT analyses of the carbide matrix interface were similar to those of the grain boundary segregation behaviour. The segregation of Ni and Si to grain boundaries has been consistently reported in irradiated austenitic steel and F-M steels [14,40–43]. The segregation of Ni can be attributed to the Inverse-Kirkendall mechanism. Si is an undersized solute and binds strongly to interstitials, leading to enrichment at the sink. It is known that phosphorus has strong segregation tendency at grain boundaries, which is thought to reduce cohesion, causing the material to fail through inter-granular embrittlement [44–47]. P segregation was also reported at the interface boundaries of precipitate/matrix type [48]. Fraction of brittle intergranular fracture correlates with P segregation level [49]. In this study, P is present in T91 as an impurity. Similarly to the previous experimental and theoretical study, P segregates to the carbide/matrix interface and its contents at the interface decreased with the increasing temperature [50,51].

Table 5 Ni, Si, Mn and P grain boundary peak concentrations (at. %) and changes (Δ) from nominal values in T91 irradiated in BOR60. The error was obtained by averaging the concentration value in the range of ± 0.6 nm from the peak position.

Irradiation condition	Ni	ΔNi	Si	ΔSi	Mn	ΔMn	P	ΔP
415 °C:18.6dpa	2.4 \pm 0.2	2.1	2.3 \pm 0.2	2.2	2.5 \pm 0.1	2.0	0.8 \pm 0.0	0.8
524 °C:15.4dpa	-	-	-	-	-	-	0.4 \pm 0.0	0.4

4.3 Fe clustering inside carbide

Fe-rich clusters were observed to form inside the carbide particle at 524 °C. This was not seen at lower temperatures. In previous studies, APT analyses of carbides after ion or neutron irradiation at temperature between 377 °C - 470 °C were shown [52,53]. Fe clustering inside carbide particles has not been reported. In the present study, the core composition of the Fe-rich clusters exceeded 80 at. %. These clusters were believed to be ferrite clusters. A noticeable difference is that the C concentration inside the carbide particle was ~ 17 at. % when irradiated at 524 °C (Figure 4 (b)). The ratio of metal/carbon exceeded the equilibrium value [54]. It is possible that the supersaturation of Fe inside carbide have caused the Fe clustering. It is known that prior to irradiation, the $M_{23}C_6$ particles were along PAGBs and lath boundaries [14]. The radiation induced enrichment/depletion of elements at PAGBs may have led to change in the Fe concentration of grain boundary and hence altering the composition of carbide particles. Irradiation has also been suggested to alter the composition of carbides [12]. Alternatively, the supersaturation of Fe inside the carbide may also exist prior to irradiation due to the fluctuation in carbide composition. Thermo-Calc with the TCFE6 database has been used to calculate the equilibrium phase inside the carbide. The actual carbide composition (~ 55 at. % Cr, 17 at. % C, 4 at. % Mo and Fe as balance) after irradiation at 524 °C was used to estimate the thermally stable phases at 524 °C. The

results confirmed the presence of ferrite under equilibrium. Irradiation could also accelerate the formation process of the Fe-rich clusters.

5 Conclusions

Atom probe tomography has offered insight into the detailed clustering and segregation behaviour of T91 steel irradiated in BOR60 reactor. The following conclusions can be drawn:

- MNS-rich clusters were observed after BOR60 irradiation at temperatures lower than 415 °C, which were not seen at higher temperatures (460 °C and 524 °C). More abundant and much smaller MNS-rich clusters were captured via APT than that of previous STEM observation, which complements the previous STEM study to provide microstructural information from different scales.
- The composition of the early stage MNS-rich clusters was characterised and compared with the thermally stable Ni-Mn-Si phases. The clusters were likely G phase precursors.
- Segregation of Ni, Si, Mn and P to the Cr-rich carbide/matrix interface was observed after BOR60 irradiation. The segregation magnitude decreased with increasing temperature. At the highest irradiation temperature 524 °C, only P segregation was detected.
- Clustering of Fe atoms inside a carbide was observed at 524 °C:15.6dpa under BOR60 irradiation.

376 6 Acknowledgement

377 This work has been supported by the IRP project fund DOE NEUP IRP under award
378 DE-NE0000639 and EPSRC EP/L025817/1. Access to the LAMDA facility at ORNL
379 was supported by the Department of Energy (DOE) National Science User Facilities
380 (NSUF) under an RTE award. This work is based upon research partially supported
381 under a DOE NEUP Graduate Fellowship. The research used UKAEA's Materials
382 Research Facility, which has been funded by and is part of the UK's National Nuclear
383 User Facility and Henry Royce Institute for Advanced Materials. Atom probe facilities
384 at the University of Oxford were supported by EPSRC EP/M022803/1. The authors
385 would like to thank Prof. Gary S. Was for helpful discussions. The authors also would
386 like to thank Dr Zhijie Jiao and Dr Kevin G. Field for preparing lift-out samples of
387 neutron irradiated T91.

388

389 Reference

- 390 [1] S.J. Zinkle, G.S. Was, Materials challenges in nuclear energy, *Acta Mater.* 61
391 (2013) 735–758. doi:10.1016/j.actamat.2012.11.004.
- 392 [2] P. Yvon, F. Carré, Structural materials challenges for advanced reactor
393 systems, *J. Nucl. Mater.* 385 (2009) 217–222.
394 doi:10.1016/j.jnucmat.2008.11.026.
- 395 [3] R.L. Klueh, A.T. Nelson, Ferritic/martensitic steels for next-generation
396 reactors, *J. Nucl. Mater.* 371 (2007) 37–52. doi:10.1016/j.jnucmat.2007.05.005.
- 397 [4] E. Getto, Z. Jiao, A.M. Monterrosa, K. Sun, G.S. Was, Effect of pre-implanted
398 helium on void swelling evolution in self-ion irradiated HT9, *J. Nucl. Mater.*
399 462 (2015) 458–469. doi:10.1016/j.jnucmat.2015.01.045.
- 400 [5] B.H. Sencer, F.A. Garner, D.S. Gelles, G.M. Bond, S.A. Maloy,
401 Microstructural evolution in modified 9Cr-1Mo ferritic/martensitic steel
402 irradiated with mixed high-energy proton and neutron spectra at low
403 temperatures, *J. Nucl. Mater.* 307–311 (2002) 266–271. doi:10.1016/S0022-
404 3115(02)01198-4.
- 405 [6] R. Schäublin, P. Spätig, M. Victoria, Microstructure assessment of the low
406 activation ferritic/ martensitic steel F82H, *J. Nucl. Mater.* 258–263 (1998)
407 1178–1182. doi:10.1016/S0022-3115(98)00182-2.

- 408 [7] C. Zheng, E.R. Reese, K.G. Field, E. Marquis, S.A. Maloy, D. Kaoumi,
409 Microstructure response of ferritic/martensitic steel HT9 after neutron
410 irradiation: effect of dose, *J. Nucl. Mater.* 523 (2019) 421–433.
411 doi:10.1016/j.jnucmat.2019.06.019.
- 412 [8] X. Jia, Y. Dai, Microstructure in martensitic steels T91 and F82H after
413 irradiation in SINQ Target-3, *J. Nucl. Mater.* 318 (2003) 207–214.
414 doi:10.1016/S0022-3115(03)00101-6.
- 415 [9] Z. Jiao, V. Shankar, G.S. Was, Phase stability in proton and heavy ion
416 irradiated ferritic-martensitic alloys, *J. Nucl. Mater.* 419 (2011) 52–62.
417 doi:10.1016/j.jnucmat.2011.08.020.
- 418 [10] S. Yamashita, Y. Yano, Y. Tachi, N. Akasaka, Effect of high dose/high
419 temperature irradiation on the microstructure of heat resistant 11Cr
420 ferritic/martensitic steels, *J. Nucl. Mater.* 386–388 (2009) 135–139.
421 doi:10.1016/j.jnucmat.2008.12.082.
- 422 [11] S. Kano, H. Yang, J. McGrady, D. Hamaguchi, M. Ando, H. Tanigawa, H.
423 Abe, Study of radiation-induced amorphization of M23C6 in RAFM steels
424 under iron irradiations, *J. Nucl. Mater.* (2020).
425 doi:10.1016/j.jnucmat.2020.152088.

- 426 [12] Z. Jiao, V. Shankar, G.S. Was, Phase stability in proton and heavy ion
427 irradiated ferritic-martensitic alloys, *J. Nucl. Mater.* 419 (2011) 52–62.
428 doi:10.1016/j.jnucmat.2011.08.020.
- 429 [13] J.P. Wharry, Z. Jiao, V. Shankar, J.T. Busby, G.S. Was, Radiation-induced
430 segregation and phase stability in ferritic–martensitic alloy T 91, *J. Nucl.*
431 *Mater.* 417 (2011) 140–144. doi:10.1016/j.jnucmat.2010.12.052.
- 432 [14] Z. Jiao, S. Taller, K. Field, G. Yeli, M.P.P. Moody, G.S.S. Was, Microstructure
433 evolution of T91 irradiated in the BOR60 fast reactor, *J. Nucl. Mater.* 504
434 (2018) 122–134. doi:10.1016/j.jnucmat.2018.03.024.
- 435 [15] P.D. Styman, J.M. Hyde, K. Wilford, A. Morley, G.D.W. Smith, Precipitation
436 in long term thermally aged high copper, high nickel model RPV steel welds,
437 in: *Prog. Nucl. Energy*, 2012: pp. 86–92. doi:10.1016/j.pnucene.2011.10.010.
- 438 [16] E.A. Little, Microstructural evolution in irradiated ferritic-martensitic steels:
439 transitions to high dose behaviour, *J. Nucl. Mater.* 206 (1993) 324–334.
440 doi:10.1016/0022-3115(93)90131-H.
- 441 [17] J. Van Den Bosch, O. Anderoglu, R. Dickerson, M. Hartl, P. Dickerson, J.A.
442 Aguiar, P. Hosemann, M.B. Toloczko, S.A. Maloy, SANS and TEM of ferritic-
443 martensitic steel T91 irradiated in FFTF up to 184 dpa at 413 °C, *J. Nucl.*
444 *Mater.* 440 (2013) 91–97. doi:10.1016/j.jnucmat.2013.04.025.

- 445 [18] E. Getto, K. Sun, A.M. Monterrosa, Z. Jiao, M.J. Hackett, G.S. Was, Void
446 swelling and microstructure evolution at very high damage level in self-ion
447 irradiated ferritic-martensitic steels, *J. Nucl. Mater.* 480 (2016) 159–176.
448 doi:10.1016/j.jnucmat.2016.08.015.
- 449 [19] B.H. Sencer, J.R. Kennedy, J.I. Cole, S.A. Maloy, F.A. Garner, Microstructural
450 analysis of an HT9 fuel assembly duct irradiated in FFTF to 155 dpa at
451 443 °C, *J. Nucl. Mater.* 393 (2009) 235–241.
452 doi:10.1016/j.jnucmat.2009.06.010.
- 453 [20] V. Kuksenko, C. Pareige, P. Pareige, Intra granular precipitation and grain
454 boundary segregation under neutron irradiation in a low purity Fe–Cr based
455 alloy, *J. Nucl. Mater.* 425 (2012) 125–129. doi:10.1016/j.jnucmat.2011.10.031.
- 456 [21] Z. Jiao, G.S. Was, Precipitate evolution in ion-irradiated HCM12A, in: *J. Nucl.*
457 *Mater.*, North-Holland, 2012: pp. 105–111. doi:10.1016/j.jnucmat.2011.12.017.
- 458 [22] M.J. Swenson, J.P. Wharry, Nanocluster irradiation evolution in Fe-9%Cr ODS
459 and ferritic-martensitic alloys, *J. Nucl. Mater.* 496 (2017) 24–40.
460 doi:10.1016/j.jnucmat.2017.08.045.
- 461 [23] J.H. Ke, H. Ke, G.R. Odette, D. Morgan, Cluster dynamics modeling of Mn-
462 Ni-Si precipitates in ferritic-martensitic steel under irradiation, *J. Nucl. Mater.*
463 498 (2018) 83–88. doi:10.1016/j.jnucmat.2017.10.008.

- 464 [24] C.L.L. Liu, G.R.R. Odette, B.D.D. Wirth, G.E.E. Lucas, A lattice Monte Carlo
465 simulation of nanophase compositions and structures in irradiated pressure
466 vessel Fe-Cu-Ni-Mn-Si steels, 1997. doi:10.1016/S0921-5093(97)00450-4.
- 467 [25] J.P. Wharry, Z. Jiao, V. Shankar, J.T. Busby, G.S. Was, Radiation-induced
468 segregation and phase stability in ferritic-martensitic alloy T 91, in: J. Nucl.
469 Mater., North-Holland, 2011: pp. 140–144. doi:10.1016/j.jnucmat.2010.12.052.
- 470 [26] C. Pareige, V. Kuksenko, P. Pareige, Behaviour of P, Si, Ni impurities and Cr
471 in self ion irradiated Fe–Cr alloys – Comparison to neutron irradiation, J. Nucl.
472 Mater. 456 (2015) 471–476. doi:10.1016/J.JNUCMAT.2014.10.024.
- 473 [27] V. Kuksenko, C. Pareige, P. Pareige, Cr precipitation in neutron irradiated
474 industrial purity Fe-Cr model alloys, J. Nucl. Mater. 432 (2013) 160–165.
475 doi:10.1016/j.jnucmat.2012.07.021.
- 476 [28] High Fidelity Ion Beam Simulation of High Dose Neutron Irradiation, Nucl.
477 Energy Univ. Progr. (n.d.). [https://neup.inl.gov/SiteAssets/FY 2013](https://neup.inl.gov/SiteAssets/FY%2013Abstracts/IRP/IRP-University%20of%20Michigan.pdf)
478 Abstracts/IRP/IRP-University of Michigan.pdf (accessed April 3, 2018).
- 479 [29] K. Thompson, D. Lawrence, D.J. Larson, J.D. Olson, T.F. Kelly, B. Gorman,
480 In situ site-specific specimen preparation for atom probe tomography.,
481 Ultramicroscopy. 107 (2007) 131–9. doi:10.1016/j.ultramic.2006.06.008.

- 482 [30] B. Gault, M.P. Moody, J.M. Cairney, S.P. Ringer, *Atom Probe Microscopy*,
 483 Springer Science & Business Media, New York, 2012.
 484 <http://books.google.com/books?hl=en&lr=&id=jSXHPIBjL1UC&pgis=1>
 485 (accessed September 25, 2014).
- 486 [31] L.T. Stephenson, M.P. Moody, P.V. Liddicoat, S.P. Ringer, New techniques
 487 for the analysis of fine-scaled clustering phenomena within atom probe
 488 tomography (APT) data., *Microsc. Microanal.* 13 (2007) 448–463.
 489 doi:10.1017/S1431927607070900.
- 490 [32] P.D. Edmondson, C.M. Parish, R.K. Nanstad, Using complimentary
 491 microscopy methods to examine Ni-Mn-Si-precipitates in highly-irradiated
 492 reactor pressure vessel steels, *Acta Mater.* 134 (2017) 31–39.
 493 <https://www.sciencedirect.com/science/article/pii/S1359645417304305>
 494 (accessed April 16, 2020).
- 495 [33] L. Messina, M. Nastar, T. Garnier, C. Domain, P. Olsson, Exact ab initio
 496 transport coefficients in bcc Fe – X (X = Cr , Cu , Mn , Ni , P , Si) dilute
 497 alloys, *Phys. Rev. B.* 90 (2014) 104203. doi:10.1103/PhysRevB.90.104203.
- 498 [34] D.J. Larson, B. Gault, B.P. Geiser, F. De Geuser, F. Vurpillot, Atom probe
 499 tomography spatial reconstruction: Status and directions, *Curr. Opin. Solid*
 500 *State Mater. Sci.* 17 (2013) 236–247. doi:10.1016/j.cossms.2013.09.002.

- 501 [35] K. Gupta, The Mn-Ni-Si (Manganese-Nickel-Silicon) System, *J. Phase*
 502 *Equilibria Diffus.* 27 (2006) 529–534. doi:10.1361/154770306x136520.
- 503 [36] P.B. Wells, T. Yamamoto, B. Miller, T. Milot, J. Cole, Y. Wu, G.R. Odette,
 504 Evolution of manganese-nickel-silicon-dominated phases in highly irradiated
 505 reactor pressure vessel steels, *Acta Mater.* 80 (2014) 205–219.
 506 doi:10.1016/j.actamat.2014.07.040.
- 507 [37] D.J. Sprouster, J. Sinsheimer, E. Dooryhee, S.K. Ghose, P. Wells, T. Stan, N.
 508 Almirall, G.R. Odette, L.E. Ecker, Structural characterization of nanoscale
 509 intermetallic precipitates in highly neutron irradiated reactor pressure vessel
 510 steels, *Scr. Mater.* 113 (2016) 18–22. doi:10.1016/j.scriptamat.2015.10.019.
- 511 [38] H. Ke, P. Wells, P.D. Edmondson, N. Almirall, L. Barnard, G.R. Odette, D.
 512 Morgan, Thermodynamic and kinetic modeling of Mn-Ni-Si precipitates in
 513 low-Cu reactor pressure vessel steels, *Acta Mater.* 138 (2017) 10–26.
 514 doi:10.1016/j.actamat.2017.07.021.
- 515 [39] N. Almirall, P.B. Wells, H. Ke, P. Edmondson, D. Morgan, T. Yamamoto,
 516 G.R. Odette, On the elevated temperature thermal stability of nanoscale Mn-
 517 Ni-Si precipitates formed at lower temperature in highly irradiated reactor
 518 pressure vessel steels, *Sci. Rep.* 9 (2019) 9587. doi:10.1038/s41598-019-
 519 45944-z.

- 520 [40] S. Zhang, X. He, T. Ko, Non-equilibrium segregation of solutes to grain
521 boundary - Part III Mechanism of non-equilibrium segregation, *J. Mater. Sci.*
522 29 (1994) 2663–2670. doi:10.1007/BF00356815.
- 523 [41] E.P. Simonen, L.A. Charlot, S.M. Bruemmer, Quantification of defect-solute
524 coupling from inverse-Kirkendall segregation, *J. Nucl. Mater.* 225 (1995) 117–
525 122. doi:10.1016/0022-3115(95)00063-1.
- 526 [42] J.P. Wharry, G.S. Was, A systematic study of radiation-induced segregation in
527 ferritic–martensitic alloys, *J. Nucl. Mater.* 442 (2013) 7–16.
528 doi:10.1016/j.jnucmat.2013.07.071.
- 529 [43] J.P. Wharry, G.S. Was, The mechanism of radiation-induced segregation in
530 ferritic–martensitic alloys, *Acta Mater.* 65 (2014) 42–55.
531 doi:10.1016/j.actamat.2013.09.049.
- 532 [44] R.G. Faulkner, S. Song, P.E.J. Flewitt, M. Victoria, P. Marmy, Grain boundary
533 segregation under neutron irradiation in dilute alloys, *J. Nucl. Mater.* 255
534 (1998) 189–209. doi:10.1016/S0022-3115(98)00022-1.
- 535 [45] S.H. Song, R.G. Faulkner, P.E.J. Flewitt, P. Marmy, M. Victoria, Grain
536 boundary phosphorus and molybdenum segregation under irradiation and
537 thermal conditions in a 2.25Cr1Mo steel, *Mater. Sci. Eng. A.* 286 (2000) 230–
538 235. doi:10.1016/S0921-5093(00)00809-1.

- 539 [46] H. Hänsel, H.J. Grabke, Grain boundary segregation of phosphorus and carbon
540 in ferritic iron, *Scr. Metall.* 20 (1986) 1641–1644. doi:10.1016/0036-
541 9748(86)90411-4.
- 542 [47] S.G. Druce, G. Gage, G. Jordan, Effect of ageing on properties of pressure
543 vessel steels, *Acta Metall.* 34 (1986) 641–652. doi:10.1016/0001-
544 6160(86)90179-3.
- 545 [48] B.A. Gurovich, E.A. Kuleshova, Y.I. Shtrombakh, O.O. Zabusov, E.A.
546 Krasikov, Intergranular and intragranular phosphorus segregation in Russian
547 pressure vessel steels due to neutron irradiation, *J. Nucl. Mater.* 279 (2000)
548 259–272. doi:10.1016/S0022-3115(00)00007-6.
- 549 [49] S.V. Fedotova, E.A. Kuleshova, D.A. Maltsev, M.A. Saltykov, Complex study
550 of grain boundary segregation in long-term irradiated reactor pressure vessel
551 steels, *J. Nucl. Mater.* 528 (2019) 151865. doi:10.1016/j.jnucmat.2019.151865.
- 552 [50] Y. Yang, S.L. Chen, Thermodynamic and kinetic modeling of grain boundary
553 equilibrium segregation of P in α -Fe, *Calphad Comput. Coupling Phase*
554 *Diagrams Thermochem.* 57 (2017) 134–141.
555 doi:10.1016/j.calphad.2017.04.002.
- 556 [51] H. Erhart, H.J. Grabke, Equilibrium segregation of phosphorus at grain
557 boundaries of Fe-P, Fe-C-P, Fe-Cr-P, and Fe-Cr-C-P alloys, *Met. Sci.* 15
558 (1981) 401–408. doi:10.1179/030634581790426877.

- 559 [52] C. Zheng, E.R. Reese, K.G. Field, T. Liu, E.A. Marquis, S.A. Maloy, D.
560 Kaoumi, Microstructure response of ferritic/martensitic steel HT9 after neutron
561 irradiation: Effect of temperature, J. Nucl. Mater. 528 (2020) 151845.
562 doi:10.1016/j.jnucmat.2019.151845.
- 563 [53] C. Zheng, M.A. Auger, M.P. Moody, D. Kaoumi, Radiation induced
564 segregation and precipitation behavior in self-ion irradiated Ferritic/Martensitic
565 HT9 steel, J. Nucl. Mater. 491 (2017) 162–176.
566 doi:10.1016/j.jnucmat.2017.04.040.
- 567 [54] M. Venkatraman, J.P. Neumann, The C-Cr (Carbon-Chromium) System, Bull.
568 Alloy Phase Diagrams. 11 (1990) 152–159. doi:10.1007/BF02841701.
- 569